

Electron emission from H_2^+ in strong laser fields

M. Odenweller,¹ J. Lower,¹ K. Pahl,¹ M. Schütt,¹ J. Wu,² K. Cole,¹ A. Vredenberg,¹ L. Ph. Schmidt,¹ N. Neumann,¹ J. Titze,¹ T. Jahnke,¹ M. Meckel,¹ M. Kunitski,¹ T. Havermeier,¹ S. Voss,¹ M. Schöffler,¹ H. Sann,¹ J. Voigtsberger,¹ H. Schmidt-Böcking,¹ and R. Dörner^{1,*}

¹*Institut für Kernphysik, J. W. Goethe Universität, Max-von-Laue-Strasse 1, 60438 Frankfurt, Germany*

²*State Key Laboratory of Precision Spectroscopy, East China Normal University, 3663 North Zhongshan Road, Shanghai 200062, China*

(Received 29 November 2013; published 31 January 2014)

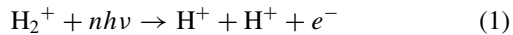
We present an experimental investigation into the angular and energy distributions of electrons set free by the interaction of hydrogen molecular ions with strong laser fields. The results extend on those presented previously [M. Odenweller *et al.*, *Phys. Rev. Lett.* **107**, 143004 (2011)] for circularly polarized light. Pulses of laser light ($\lambda = 780$ nm, $I \approx 6 \times 10^{14}$ W cm⁻², $\tau \approx 40$ fs) of both linear and circular polarization are focused onto an H_2^+ molecular ion beam. The momenta of the proton and electron fragments are determined in a coincidence experiment, enabling electron momentum emission patterns in the molecular frame to be deduced for specific values of internuclear distances.

DOI: [10.1103/PhysRevA.89.013424](https://doi.org/10.1103/PhysRevA.89.013424)

PACS number(s): 33.80.Rv, 32.80.Rm, 42.50.Hz

I. INTRODUCTION

H_2^+ , the simplest of all molecular ions, provides the ideal test case to enhance our understanding of molecular ionization processes. As H_2^+ is a single-electron system, all features arising from the two-center nature of the problem can be cleanly studied in the absence of electron-electron interaction. For ionization by single-photon impact the most prominent effect is two-center interference. For multiphoton and strong-field ionization of a molecular target a large number of interesting effects emerge, such as the mapping of molecular orbitals [1] and laser-induced electron diffraction [2]. In all cases the reaction



has a twofold significance; it allows the dynamics of the prototype molecular ion H_2^+ to be probed and allows basic properties of laser ionization to be investigated. Because of this fundamental relevance, theoretical studies on strong-field ionization frequently employ the hydrogen molecular ion as a target (see, for example, [3–11]). In contrast, experimental investigations into this special reaction are quite scarce and have concentrated exclusively on the nuclear dynamics [12–17]. The current experiment is the first to measure the ionized electron in addition to the nuclear fragments, enabling the electron dynamics to be directly investigated and the interplay between nuclear and electronic degrees of freedom to be sensitively explored. Some selected results for circularly polarized laser light obtained with the experimental apparatus described here were reported earlier [18]. Here we put special emphasis on the experimental technique and on ionization by linearly polarized light.

A. Ionization mechanism

For the laser intensities employed in the present measurement, the dominant ionization mechanism for H_2^+ is charge resonance enhanced ionization (CREI). It leads to a

large enhancement of the molecular ionization rate for certain critical internuclear separations R , which are predicted to peak near 6 and 10 a.u. for H_2^+ [5–7,19]. The enhanced ionization probability is due to a strong coupling between the $1s\sigma_g$ electronic ground state and the $2p\sigma_u$ first excited state of the hydrogen molecular ion, which form a charge-resonance pair. When the laser interacts with H_2^+ , the bound electron experiences a new potential resulting from the combined actions of the laser field and the Coulomb potential of the nuclei. For a laser polarization aligned along the molecular axis, this results in two potential wells located on a laser-dependent incline which changes its slope and direction with the laser frequency. The presence of the charge-resonance pair of states and the nonadiabatic nature of the laser excitation leads to a significantly increased population at the uphill nucleus, which can tunnel through or proceed over the inner barrier between the nuclei with very high probability. This preferred emission of electrons from the up-field side of the molecule has recently also been established experimentally [20]. CREI can be approximated as a quasistatic phenomenon because although the population located at the upper nucleus is due to a dynamic process, ionization occurs within a time frame much smaller than the period of a single laser cycle. However, evidence for breakdown of the quasistatic picture has recently been presented by calculation [21,22] and through a comparison of calculations with our experimental results for circularly polarized light [18].

At the instant of ionization t_i , the emitted electron possess a small value of momentum \vec{p}_{initial} due to its motion within the target. Often, the laser field is so strong and the electron is set free at such a large distance from the nuclei that their mutual Coulomb interaction can be neglected [strong-field approximation (SFA)]. Neglecting any initial momentum for the emitted electron and any postionization interaction between it and the nuclei, its trajectory can be described by the classical equations of motion for an electron in the electric field of intense laser light [23]. After ionization, the two bare protons leave the ionization center in a Coulomb explosion.

For linear polarization, under certain circumstances, the electron can be driven back to the nuclei and rescatter. For elliptical or circular polarization, however, rescattering

*doerner@atom.uni-frankfurt.de

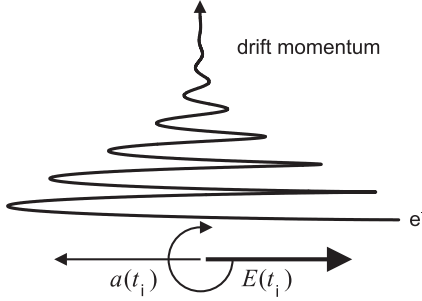


FIG. 1. Trajectory of an electron with zero initial momentum ionized at time t_i by a clockwise-rotating circularly polarized laser pulse. The pulse propagation direction is directed into the page. The asymptotic direction of the electron drift momentum \vec{p}_{end} is perpendicular to that of the electric field $\vec{E}(t_i)$ and its acceleration $\vec{a}(t_i)$ at the instant of ionization.

cannot occur. In the absence of rescattering the final electron momentum \vec{p}_{end} , achieved after the pulse has faded away, depends only on the vector potential $\vec{A}(t_i)$ of the laser at the instant of ionization:

$$\vec{p}_{\text{end}} = \vec{p}_{\text{initial}} - e \cdot \vec{A}(t_i). \quad (2)$$

Approximating $\vec{p}_{\text{initial}} = 0$ and with e representing the elementary charge, the magnitude and direction of the electron's final momentum only depends on $\vec{A}(t_i)$. $\vec{A}(t)$ is related to the electric field through the equation

$$\vec{E}(t) = -\frac{\partial}{\partial t} \vec{A}(t). \quad (3)$$

This leads to a final electron momentum directed along the polarization axis and of maximum value

$$p_{\text{max}} = \frac{eE_0}{\omega}, \quad (4)$$

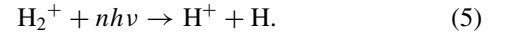
where E_0 is the maximum value of electric field reached within the pulse. p_{max} is reached for electron tunneling occurring in the limit of the oscillating electric field approaching a zero crossing, i.e., when $|\vec{E}(t_i)| \rightarrow 0$. The ionization probability, however, tends to zero in this case. Ionization at phases of maximum electric field occur with highest ionization probability, and if the envelope does not change significantly during one laser cycle, $\vec{A}(t_i) = \vec{p}_{\text{end}} = 0$ for this case.

For circular polarization comprising orthogonal field components, in contrast, the action of the vector field leads to an electron momentum \vec{p}_{end} pointing at 90° with respect to the electric field at the instant of ionization $\vec{E}(t_i)$ [24]. The direction of this perpendicular drift momentum is determined by the helicity of the laser field. Figure 1 shows its helicity-dependent sense when measured with respect to $\vec{a}(t_i) \propto -\vec{E}(t_i)$. An improvement to the above “free-electron” model, first proposed by van Linden van den Heuvell and Muller [25], is achieved by ascribing an initial momentum \vec{p}_{initial} to the emitted electron. The acceleration of an electron, within a nonrelativistic laser field, proceeds at all times along the field direction; there is no momentum transfer in the direction perpendicular to the electric field. Hence, the distribution of electron momenta in the direction perpendicular to the polarization direction (linear) or polarization plane (circular polarization) reflects the distribution of electron momenta at the exit of the tunnel

(this was exploited in [2] to trace out molecular orbitals in momentum space). Nevertheless, even without accounting for initial electron momenta, the model has been shown to give good results on various occasions [1,26,27]. In this article we show that the free-electron model does not apply in the case of H_2^+ in circularly polarized light at internuclear separations beyond 5 a.u.

B. Interplay of ionization and dissociation mechanisms

Dissociation is generally defined as the process by which a molecule fragments into smaller atomic or molecular products. Here we restrict the term dissociation to fragmentation processes driven by excitation of the parent molecule, excluding those initiated through its ionization, namely,



For H_2^+ in a laser field, dissociation results from the strong laser coupling of the $1s\sigma_g$ ground state with the first excited $2p\sigma_u$ state. At low laser intensities, the probability for dissociation exceeds that for ionization and may assume appreciable values even below intensities of $10^{14} \text{ W cm}^{-2}$. As a result, the molecular ion will begin to dissociate on the leading edge of a laser pulse before its subsequent ionization closer to the pulse-envelope maximum. The dissociation mechanism itself has been previously extensively analyzed by both experiment and theory [16,28–41]. The two main processes leading to dissociation are bond softening (BS) and bond hardening (BH). For the latter, dissociation starts at the falling edge of the laser pulse [36], which disqualifies it as a preionization mechanism. That leaves BS as the main precursor dissociation process. The angular dependency of this process is confined in a small angular region around the polarization axis [38].

As described earlier, the dominant process leading to ionization, under the experimental conditions of this work, is CREI. As the strength of this process depends sensitively on the internuclear distance R_{ion} at the instant of ionization, understanding its R dependence is of considerable interest. While it is not possible to measure R_{ion} directly, its value is closely related to the magnitude of kinetic energy gained by the two residual protons liberated through the ionization process, the so-called kinetic energy release (KER). KER is determined by our measurement. Due to the uncertainty relation between position and momentum, even with exact knowledge of the internuclear potential, a particular value of KER cannot be ascribed to a specific value of R_{ion} ; nevertheless the measured value of KER can be used to provide an approximate measure of the region of coordinate space in which values of R_{ion} are localized at the instant of ionization [42]. Small (large) values of KER typically correspond to ionization at large (small) internuclear distances.

The most probable excitation leading to dissociation and resulting from BS occurs near the one-photon resonance of the $1s\sigma_g$ and $2p\sigma_u$ hydrogen molecular ion states at an internuclear separation of 4.7 a.u. For dissociation commencing at this particular R value and proceeding along the $2p\sigma_u$ potential energy curve, an internuclear separation of 7 a.u. is reached in about 10 fs. Thus, given the relatively long 40-fs pulse length employed in the present work, it is possible for the dissociating nuclei to separate to a considerable distance before the peak

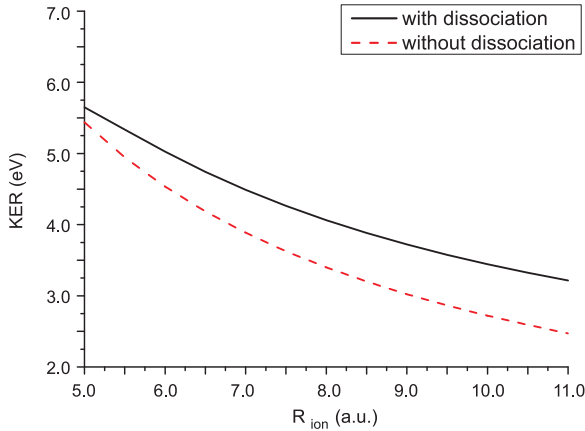


FIG. 2. (Color online) Dependency of KER on the internuclear separation R_{ion} at the instant of ionization. Red dashed line: without consideration of a precursor dissociation. Black solid line: precursor dissociation taken into account.

of the laser-pulse envelope is reached, in whose neighborhood ionization is most probable. As a result, the distribution of internuclear separations at the instant of ionization exhibits greater values than would be expected from the spatial extent of the wave functions associated with the vibrational-level distribution of the H_2^+ electronic ground state alone. Thus, for dissociation commencing at an internuclear separation R_{diss} the measured KER comprises separate contributions from the energy ($E_{\text{KER,diss}}$) gained by the protons as they translate along the $2p\sigma_u$ potential energy curve prior to ionization and from the energy ($E_{\text{KER,ion}}$) they gain through their mutual Coulomb repulsion as they recede from each other after ionization:

$$E_{\text{KER}} = E_{\text{KER,diss}} + E_{\text{KER,ion}}. \quad (6)$$

The contribution $E_{\text{KER,diss}}$ is generally much smaller than $E_{\text{KER,ion}}$. The higher the overall E_{KER} (ionization at smaller internuclear distances) is, the smaller the relative contribution to it from $E_{\text{KER,diss}}$ is. The value of $E_{\text{KER,diss}}$ is approximately 0.2 eV for $R_{\text{diss}}=5$ a.u., 0.6 eV for $R_{\text{diss}}=7$ a.u., and up to 0.7 eV for higher distances. Using the well-known R dependence of the internuclear potential for the $2p\sigma_u$ state and taking the Coulomb repulsion between two bare protons into account, internuclear separations R_{ion} can be assigned to specific values of KER. Figure 2 shows the assignment of R_{ion} to KER with and without the effects of a foregoing dissociation considered. As stated earlier, values derived from this assignment are approximate due to the uncertainty relation between position and momentum.

II. EXPERIMENT

Due to the effects of space charge [43], measurements employing ion beams are generally more challenging than analogous measurements employing neutral-beam targets. The space charge limits the maximum beam density achievable, resulting in reduced signal rates. Furthermore, at significantly lower beam densities than the space-charge-limited maximum, space-charge-induced smearing out of energy-resolved structures [44] can occur, limiting permissible target densities to even lower values.

For the present experiment a 22 nA/mm target beam was employed, corresponding to a target density of 2.4×10^6 ions/cm³. For a laser focus volume of around 1.4×10^{-6} cm³ this corresponds to 0.03 H_2^+ ions. In contrast, the laser focus volume contains around four molecules of background gas arising from the background pressure of 1×10^{-10} mbar prevailing in the reaction chamber. Without measures to suppress the electron signal from ionized background gas, a signal-to-background ratio of less than 1:100 would therefore be expected. The challenge to the present measurement was thus clear: the development of a powerful method to suppress electron background signal would be needed to obtain reliable spectra. How this was achieved is explained in the following paragraphs.

Our experimental setup consists of three distinct sections. These comprise (i) a Van de Graaff accelerator to generate a target beam of H_2^+ ions in their electronic ground state, (ii) a Ti:sapphire femtosecond laser system to generate ultraintense light pulses, and (iii) experimental chambers in which the photon and ion beams are crossed to induce ionization and fragmentation and in which the emerging bare proton and electron products are momentum analyzed in a coincidence measurement. The Van de Graaff accelerator and experimental chambers are now described in more detail.

A. Van de Graaff accelerator

The experiment was performed using the Van de Graaff accelerator of the Stern-Gerlach-Zentrum in Frankfurt am Main, which provided a beam of H_2^+ ions in their electronic ground state. The ions were formed in a high-frequency ion source via electron impact ionization of H_2 molecules in their electronic ground state. After extraction and acceleration by electrostatic fields and after mass-charge selection and focusing through various carefully fashioned magnetic-field configurations, the ion beam enters the collision chamber located at a distance 23.4 m away. H_2^+ molecular ions entering the collision chamber are necessarily in their $1s\sigma_g$ electronic ground state as the H_2^+ ions formed in their excited electronic states are unstable and dissociate rapidly in transit. The population distribution of vibrational levels in the molecular ion ensemble corresponds to a Franck-Condon-like population distribution [45].

B. Experimental chambers

Figure 3 shows an overview of the experimental chambers. They consist of a differential-pumping stage, a reaction chamber, and a drift region.

1. Differential-pumping stage

The differential-pumping stage assists in establishing a large pressure gradient between the ion source and the reaction chamber. High pumping speeds are achieved by the combined application of turbomolecular pumps and a cryopanel. Tubes located along the ion-beam axis at the entrance and exit of this chamber are employed to further reduce gas flow from the ion source into the reaction chamber where a background pressure of 1×10^{-10} mbar is achieved by a combination of turbo-, cryo-, and sublimation pumps.

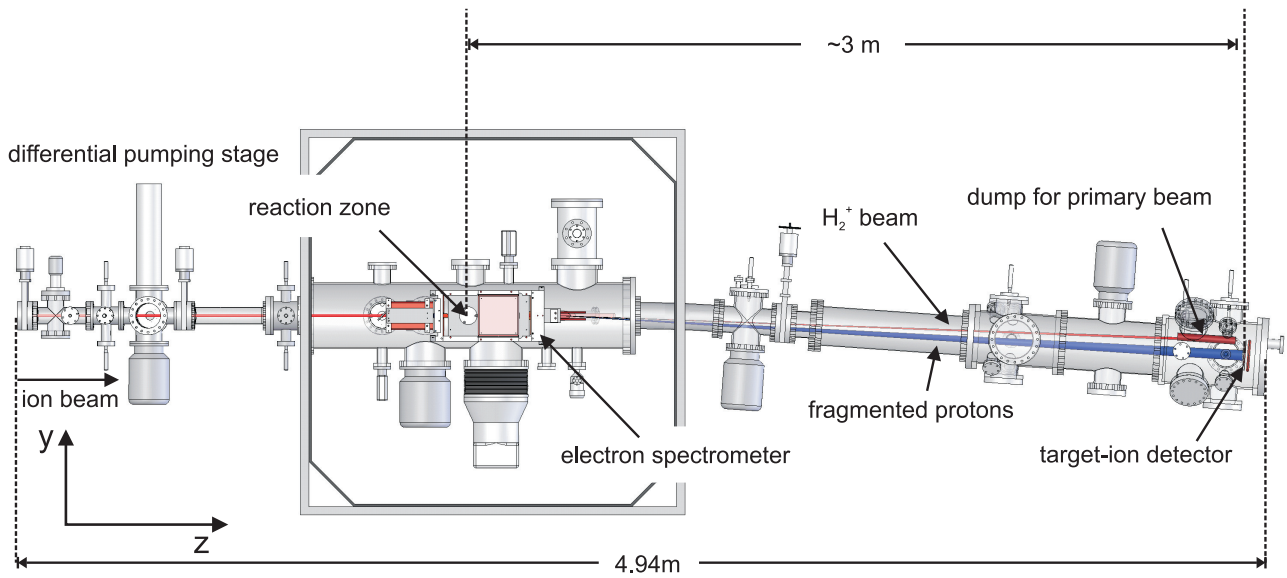


FIG. 3. (Color online) Overview of the experimental setup. The reaction zone, defined by the overlap of H_2^+ and laser beams, is located inside the electron spectrometer, where a homogeneous electric field is applied. The target-ion detector is located at a distance of 3 m behind the reaction zone. Compensation for the earth's magnetic field is achieved by externally mounted Helmholtz coils.

2. Reaction chamber

After leaving the differential-pumping stage, the ion beam enters the reaction chamber, where it is overlapped with and ionized by an 8-kHz train of 40-fs, 780-nm laser pulses of intensity $I \approx 6 \times 10^{14} \text{ W cm}^{-2}$ of either linear or circular polarization. The overlap of photon and ion beams defines the reaction zone which is located within the electron spectrometer, where a homogeneous electric field guides electrons onto a position- and time-sensitive detector.

The detection of electron and ion fragments over the full 4π emission solid angle and the reconstruction of their momenta is achieved through a variant of the so-called cold target recoil ion momentum spectroscopy (COLTRIMS) technique [46]

adapted specifically for the present laser-ion study. The electron spectrometer is shown schematically in Fig. 4.

In its first stage (the so-called beam cleaner) a uniform electric field \vec{E}_c is employed to separate projectile H_2^+ ions from protons and neutral H_2 molecules generated upstream through charge transfer between H_2^+ ions and background molecules.

In the second stage, a second uniform electric field \vec{E}_e guides electrons onto two detectors. As previously noted, a major challenge to the experimental design was to ensure that background electrons resulting from residual-gas ionization were effectively suppressed. Such electrons possess the same time of flight (TOF) to the electron detectors, measured relative

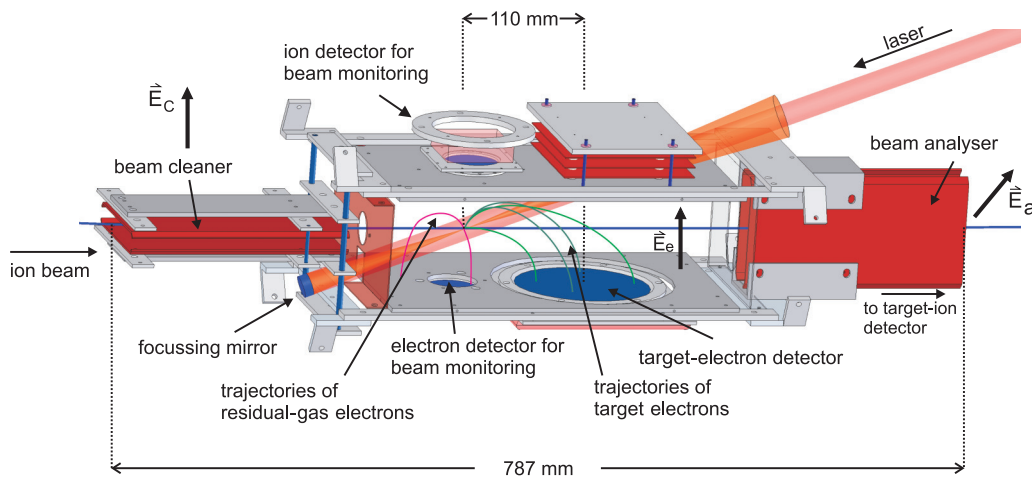


FIG. 4. (Color online) Sketch of the electron spectrometer. Stage 1: The H_2^+ projectile beam is separated from protons and neutral H_2 molecules, generated through its interaction with background gas, by the field \vec{E}_c . Stage 2: A laser beam crosses the H_2^+ beam, and field-forming electrodes located inside the spectrometer (omitted to improve visibility) produce a uniform electric field \vec{E}_e to guide ionized electrons onto the target-electron detector. Stage 3: A third electric field \vec{E}_a spatially separates fragment protons from projectile ions and guides them to the target-ion detector.

to the arrival time of the laser pulse, as electrons emitted from target molecules. This makes them indistinguishable without an additional means of labeling. Distinguishability is achieved by exploiting the velocity $v = 2.81$ a.u. of the H_2^+ ions, which provides an offset momentum for the electrons emitted from them; electrons released through the ionization of the quasistationary background-gas molecules do not possess this momentum offset. This momentum offset results in a spatial separation of electrons derived from fast-moving H_2^+ (detected on the target-electron detector) from those emitted through the ionization of background gas (detected on the beam-monitoring electron detector).

The target-electron detector comprises a quadratic DLD120 detector of 120-mm active diameter manufactured by Roentdek (for details on the detector system see [47,48]). Its mounting position is offset from the reaction zone by 110 mm along the ion-beam axis to account for the component of momentum received by the electrons due to the velocity of the H_2^+ ions from which they are launched (see Fig. 4). In contrast, electrons released through the ionization of background gas are focused onto a region centered directly below the reaction zone where the beam-monitoring electron detector is located. It is pertinent to note that for circularly polarized light, emitted electrons gain momentum from the laser field exclusively within the polarization plane. For this reason the laser beam was inclined by a shallow angle of 20° to the ion-beam axis. This ensured that the component of momentum transferred to electrons from the laser field along the ion-beam axis remained sufficiently small that electrons derived from target- and background-gas ionization did not spatially overlap. For linearly polarized light, emitted electrons gain momentum from the laser field in a direction parallel to the polarization axis. To avoid overlap in this case, the polarization axis was aligned parallel to the detector plane to render the component of momentum transferred to electrons from the laser field along the ion-beam axis zero. The offset of the electron detector, the shallow impingement angle of the laser beam, and the alignment of the spectrometer focusing field perpendicular to the ion-beam axis ensured that only electrons with the initial velocity of the ions arrived at the DLD120 detector (Fig. 4). With an adopted electric-field strength of $E \approx 35.7$ V cm $^{-1}$ the TOF of the electrons was ~ 12 ns. As a result of the low TOF value the component of momentum resolution along the axis of the guiding electric field had a relatively modest value, with $\Delta p_{e,x} = 0.18$ a.u. Superior momentum resolution was achieved for components of momentum measured along axes perpendicular to the guiding field: $\Delta p_{e,y} \approx \Delta p_{e,z} = 0.07$ a.u.

After ionization the H_2^+ molecule breaks apart due to the mutual Coulombic repulsion of the two bare protons. These subsequently pass through the final stage of the electron spectrometer, the so-called beam analyzer, in which a third uniform electric field \vec{E}_a is employed to spatially separate protons from projectile ions and deflect them in the direction of the fragment-ion detector.

3. Drift region and target-ion detector

Upon leaving the electron spectrometer the protons traverse a 3-m-long drift region in which they separate from one

another, both spatially and temporally, before impinging on the fragment-ion detector comprising a Roentdek HEX75 [47] hexagonal position- and time-sensitive detector of 75-cm active diameter. By measuring the momenta of the two protons in time coincidence the alignment of the molecular axis at the instant of ionization can be inferred as the fragments fly apart back to back. For the protons, as was the case for the electrons, the components of momentum resolution parallel to the detector surface $\Delta p_{p,x} = \Delta p_{p,y} = 0.5$ a.u. are much smaller in magnitude than for the component in the orthogonal direction, with $\Delta p_{p,z} = 3.2$ a.u. The rate of protons detected within a time window of 3.2 ns around the central TOF value of 476 ns is about 64 Hz. Some 93% of these protons originate from laser-induced dissociation of H_2^+ ; the overall predominance of protons originating through dissociative excitation over dissociative ionization is due to the considerably lower laser-intensity threshold for the former process. As a result a much larger volume of the laser focus triggers dissociation compared to ionization. Determined through a twofold coincidence measurement of a proton and the corresponding tunnel-ionized electron, the measured coincidence rate for dissociative ionization was around 1 Hz.

4. Beam alignment

Given the extremely dilute nature of the H_2^+ target beam, aligning it with the laser focus and monitoring the stability of experimental conditions presented a nontrivial

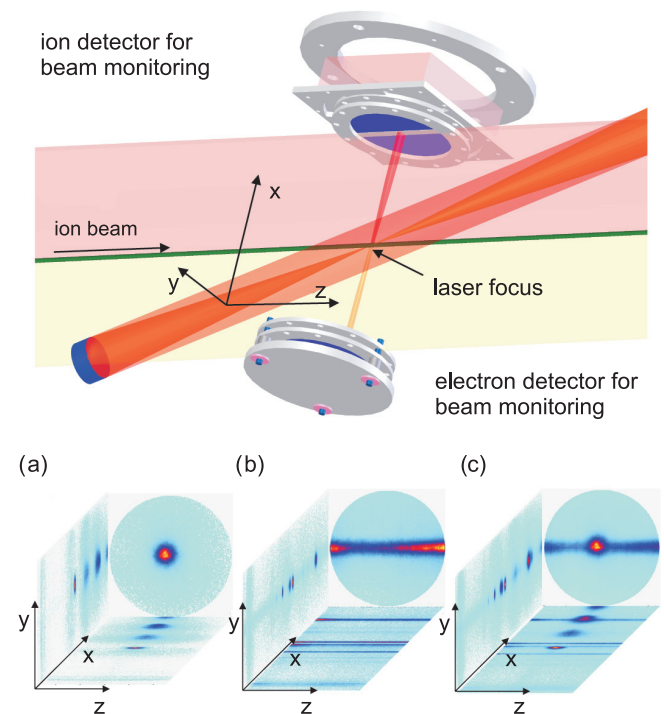


FIG. 5. (Color online) (top) Depiction of the beam-monitoring arrangement. Laser and ion beams produce ion-electron pairs which are guided to the monitoring detectors by an applied electric field. (bottom) Images produced by the beam monitoring system: (a) only laser beam present in reaction chamber, (b) only ion beam present in reaction chamber, and (c) both ion and laser beams present in the chamber.

problem. For this reason, the setup was equipped with an additional set of two detectors centered about the reaction zone. These are referred to as “monitoring detectors.” One is a position- and time-sensitive DLD40 detector negatively biased to detect ions; the other is a time-of-flight-only electron detector (Figs. 4 and 5). The primary H_2^+ ion beam and the laser beam randomly ionize molecules of residual gas which produce ion-electron pairs that are measured on these two detectors. Because of the applied electric field in this region, fragment ions derived from residual gas are focused onto the beam-monitoring ion detector and generate two-dimensional projections of the ion and laser beams and of the laser focus. Determination of the beam positions in the third (y) dimension is obtained by measuring the detection times of ions with respect to those for their associated tunnel-ionized electrons, which are detected in time coincidence. Assignment of measured times of flight to specific y position values and identification of various peaks in the TOF spectrum corresponding to different background-gas molecules was achieved by calibrating the time scale using ^{40}Ar , which was separately injected into the reaction chamber. In this way an optimum overlap of laser and ion beams and a sensitive monitoring of experimental conditions were achieved.

III. RESULTS AND DISCUSSION

A. Linear polarization

1. Proton momenta and energy distributions

Here we consider the momentum distributions of electrons and protons derived from the ionization and subsequent fragmentation of H_2^+ induced by linearly polarized light. These distributions enable underlying mechanisms of molecular ionization and fragmentation to be carefully investigated. Figure 6 shows the momentum distribution of protons when the laser-field polarization is aligned along the y axis. Figure 6(a) shows events corresponding to proton arrival times t_{pr} where

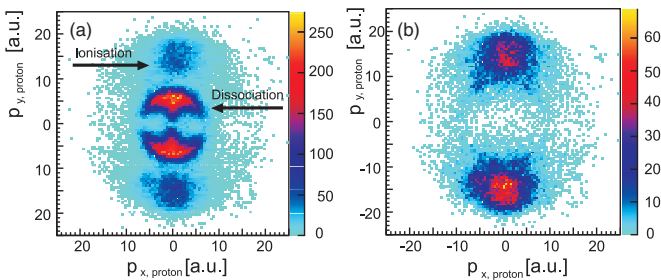


FIG. 6. (Color online) Proton momentum distribution for the photoionization and photodissociation of H_2^+ by linearly polarized light aligned along the y axis. The laser intensity $I \approx 6 \times 10^{14} \text{ W cm}^{-2}$. (a) Events corresponding to proton arrival times t_{pr} where $474 \text{ ns} < t_{pr} - t_i < 479 \text{ ns}$. In the inner region ($|p| < 10 \text{ a.u.}$) the typical anchor-like structure of dissociation [49] is visible; events at higher momentum values correspond to ionization. (b) Same as (a), except with the additional constraints (i) on the electron arrival time t_e ($8 \text{ ns} < t_e - t_i < 17 \text{ ns}$) and (ii) on the magnitude of the proton momentum $|p|$ ($|p| < 9 \text{ a.u.}$). These constraint suppress background events and those corresponding to the dissociation process.

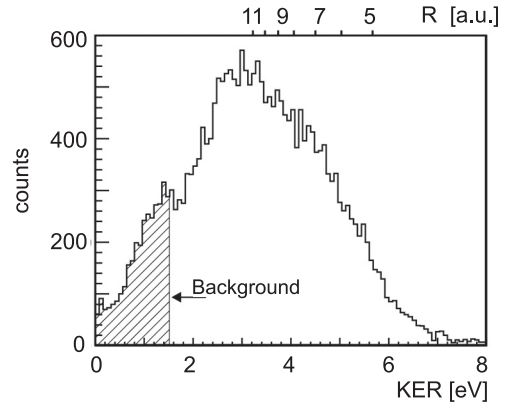


FIG. 7. KER distribution for linearly polarized laser pulses. Ascribed internuclear separations are shown at the top.

$474 \text{ ns} < t_{pr} - t_i < 479 \text{ ns}$. Evident in the inner region is a typical anchor-like structure [49] arising from a combination of BS and BH, associated with the dissociation of H_2^+ into H and H^+ fragments. In the outer-region contributions between 10 and 20 a.u. (KER values between 1.5 and 6 eV) are associated with the Coulomb explosion of two H^+ ions following an ionization event. In Fig. 6(b) additional constraints are applied to the electron arrival time t_e , where $8 \text{ ns} < t_e - t_i < 17 \text{ ns}$, and to the magnitude of the proton momentum $|p|$, namely, $|p| < 9 \text{ a.u.}$ These result in suppression of background events and those corresponding to dissociation, enabling contributions from laser-induced ionization to be cleanly separated out. Evident in both panels is a clear preference for ionization to occur when the laser polarization axis and the H_2^+ intermolecular axis are closely aligned. However, as the ionization pattern is weighted with the angular dependency of the BS precursor dissociation process, which itself is confined to a small angular region around the polarization axis [49], it is not obvious to what extent the observed distribution simply reflects the BS angular dependency. Nonetheless, it is reasonable to expect that the ionization probability even in the absence of BS would also us to show a directed distribution, as the impact of CREI is expected to be the greatest for the molecular axis aligned parallel to the laser field.

Figure 7 shows the distribution of KER, derived from the data in Fig. 6(b), associated with ionization events which were determined by exclusively selecting proton pairs for which an electron was detected in time coincidence. Internuclear distances are ascribed to specific KER values using the solid curve of Fig. 2. The maximum of the event rate occurs around 3 eV. Low-energy KER contributions below 1.5 eV arise predominantly from false coincidences, which could not be effectively suppressed in the present experiment due to the high prevailing dissociation (proton) rate in this KER range. Very few events are seen to occur for KER values above 6 eV (internuclear separations smaller than 5 a.u.). The distribution shows evidence of a shoulder at around 7 a.u. Considering the corresponding internuclear separation, this can be attributed to CREI, which predicts that the ionization rate will significantly increase at critical internuclear distances of 6 and 10 a.u. In contrast to expectations based on CREI considerations alone, no two well-resolved CREI peaks are visible. However, as

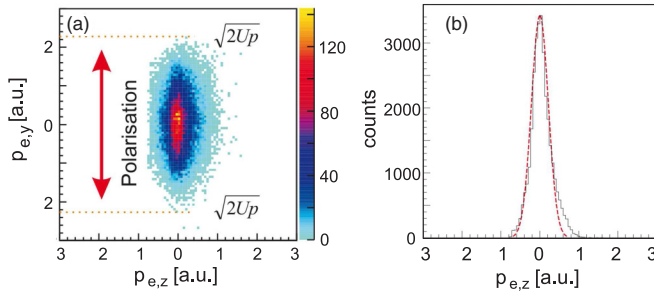


FIG. 8. (Color online) (a) Electron momentum distribution as a function of the two momentum components $p_{e,y}$ and $p_{e,z}$ in the y - z detector plane, which is aligned parallel to the axis of polarization. As predicted by the free-electron model, momenta values lie within the bounds $\sqrt{2U_p}$, where U_p represents the ponderomotive potential for linearly polarized light. (b) Electron momentum distribution as a function of the z momentum component. The dashed orange line is the result of a calculation using the so-called Ammosov, Delone, and Krainov (ADK) theory [50].

described earlier, the assignment of KER values to specific internuclear separations is limited by a broadening associated with the Heisenberg position-momentum uncertainty relation.

2. Electron momenta and energy distributions

Having discussed the momenta and energy distributions related to protons released from the photon-induced fragmentation of H_2^+ , we now turn our attention to those describing the associated electron emitted through tunnel ionization. Relative to the protons, the tunnel electrons span a much smaller range of momenta values which are, in the present measurement, determined to a considerably higher level of absolute precision. This enabled us to resolve a much finer momentum structure than would have been possible from studying the proton spectra alone.

Figure 8(a) shows the dependence of the fragmentation rate of H_2^+ on the magnitude of the electron momentum components in the y - z detector plane. The axis of linear polarization, which lies parallel to this plane, is indicated by the double-ended arrow. Data presented in Fig. 8(a) represent an integration over directions for proton emission, i.e., over all molecular-axis alignment directions. The first point to note is the greater range of momentum values for electrons emitted along the polarization direction compared to those emitted along the axis orthogonal to it. This can be accounted for by the fact that momentum transfer from the laser field to the tunnel electron occurs exclusively along the field direction. The measured values for momentum components along this direction are seen to lie within the bounds $\sqrt{2U_p}$, where U_p represents the ponderomotive potential for linearly polarized light. The bounds $\sqrt{2U_p}$ are predicted by the free-electron model described in Sec. I, in which the interaction of the tunnel electron with the nuclei is ignored and the initial electron momentum at the instant of ionization is neglected. Further, the following two observations are also consistent with that model. First, a maximum of intensity is seen at a zero value for the longitudinal component of the electron momentum. This is accounted for by those ionization events which occur at phases

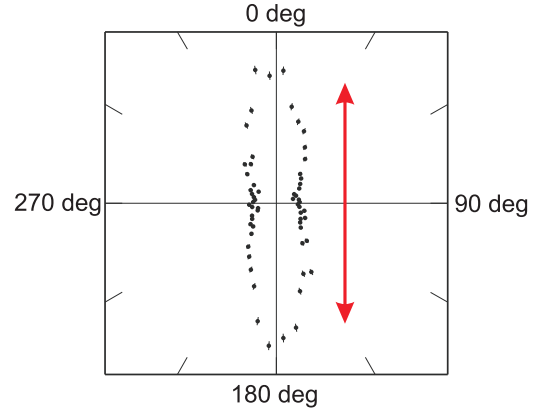


FIG. 9. (Color online) Electron angular distribution in the y - z detector plane aligned parallel to the axis of polarization, as indicated by the double-sided arrow.

of the driving electric field corresponding to local maxima of electric-field strength. There the ionization probability is at its greatest, and the momentum transfer to the tunnel electron is zero. Second, the spread in values of the longitudinal component of the electron momentum can be explained by the spread in the values of the phase- and envelope-dependent laser field strength at the instants when ionization occurs, ranging between values of zero and E_0 . Not accounted for within the free-electron model is the observed finite width of the electron momentum distribution along the direction perpendicular to the polarization axis, which is highlighted in the representation of Fig. 8(b). This observation, however, can be explained by additionally assuming that a finite-width momentum distribution is present at the exit of the tunnel process [51].

Figure 9 shows an integration of the same data used in Fig. 8 to present the results in a polar plot. Here the distance of each data point from the origin is proportional to the cross section for tunnel ionization, and the angle made by the line joining the data point to the origin, referenced to the y axis, represents the electron emission direction with respect to the axis of laser polarization. This rendering of the data highlights the preference for electron emission to occur along the axis of laser polarization. In combination with the findings of Fig. 6, an overall picture of the process is obtained: a strong preference for ionization to occur when the molecular axis is aligned to the laser field and for the ionized electron to be driven in directions concentrated around the polarization axis.

Figures 10(a) and 10(b) show the dissociative-ionization rate as a function of the components of emitted-electron momenta perpendicular and parallel to the polarization axis, respectively, for various ranges of KER. The results for different KER regions are normalized to one another. For the momentum component p_z aligned perpendicular to the polarization axis [Fig. 10(a)], the shapes of the distributions are essentially independent of the KER regions considered. This is unsurprising as momentum transfer from the laser field to the emitted electron is zero in this perpendicular direction, and therefore, no dependence on KER (R) is to be anticipated. Even for the lowest KER region from 1.5 to 2 eV, where

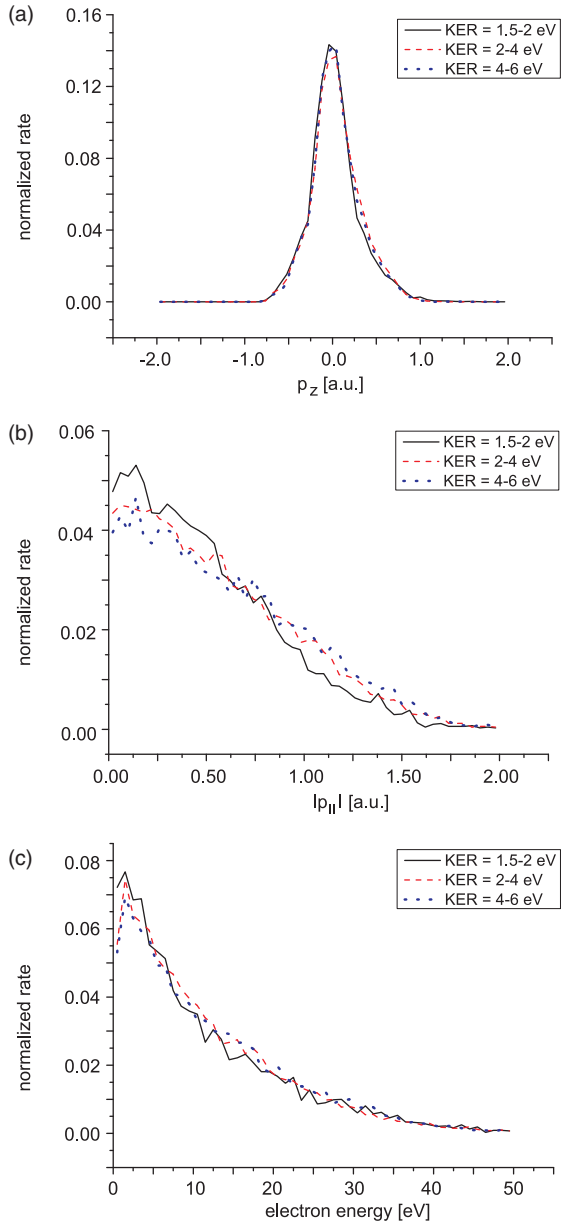


FIG. 10. (Color online) Normalized count rates for dissociative ionization of H_2^+ measured with linearly polarized 40-fs laser pulses ($I = 6 \times 10^{14} \text{ W cm}^{-2}$). (a) Count rate as a function of the emitted-electron momentum component along the z axis, which is aligned perpendicular to the laser-polarization direction. (b) Count rate as a function of the component of emitted-electron momentum along the laser polarization direction. (c) Emitted-electron energy distribution. The graphs show three different KER regions: 1.5–2 eV, black straight lines; 2–4 eV, red dashed lines; and 4–6 eV, blue dotted lines.

ionization occurs at very large ($R > 20$ a.u.) internuclear separations, the spectrum shape remains essentially unchanged within experimental error.

For the distributions corresponding to momentum component $p_{||}$ aligned parallel to the polarization axis [Fig. 10(b)], the results for the lowest KER region diverge slightly from those corresponding to higher KER values, with the distribution exhibiting a slightly narrower full width at half maximum. This narrowing can be attributed to the lower laser intensity

experienced by H_2^+ molecules at the time of ionization t_i when ionization occurs at large internuclear distances following precursor dissociation. For the present case of a 40-fs pulse length, this corresponds to ionization occurring at the falling edge of the laser pulse.

Figure 10(c) shows the measured kinetic-energy distribution for the emitted tunnel electrons. A slightly narrower distribution is observed for the range of KER with the smallest values, which again is probably attributable to the propensity for ionization to have occurred at the falling edge of the laser pulse for large- R cases. This would result in a smaller transfer of momentum to the emitted electron from the laser field due to it experiencing a lower average laser intensity at the time of ionization t_i . Overall, however, it is observed that the internuclear separation has relatively little influence on the final momentum of the ionized electron.

B. Circular polarization

For the case of linear polarization, the electric field vector is confined to an axis, and its strength oscillates harmonically in time. In contrast, a state of circular polarization is described by a superposition of two linearly polarized waves of the same frequency with a relative phase of $\pi/2$. This results in an electric field vector which is confined to a plane normal to the photon propagation direction, which assumes special significance in the outcome of photon-driven processes. For this reason we adopt here a new coordinate system (x', y', z') in which to analyze the data for circularly polarized light (see Fig. 5). It is achieved by performing a rotation around the y axis by 20° (the laser tilt angle). The resultant x' - y' (x' - y') plane coincides with the polarization plane, and the z' axis is aligned perpendicular to it. In the limit of infinite pulse duration, in contrast to linear polarization, $|\vec{E}(t)|$ remains constant with time, and no time instant exists where $|\vec{E}(t)| = 0$. The constant-magnitude electric-field vector continuously changes direction, rotating in the polarization plane with the frequency ω of the laser (in the present study, employing a pulse of finite length, the electric-field strength varies according to the form of the pulse envelope). Furthermore, whereas for linear polarization the molecular ionization probability depends on the angle between the molecular and polarization axes, for circular polarization it depends on the angle between the molecular axis and the polarization plane.

In Sec. I we described how electrons, tunnel ionized from molecules through the action of circularly polarized light, gain a momentum which depends on the magnitude of the electric field at the time of ionization t_i (free-electron model). With the assumption of an instantaneous tunnel ionization with greatest probability when \vec{E} is aligned with the molecular axis and an initial electron momentum close to zero, one would expect to observe final electron momenta of well-defined magnitudes corresponding to the narrow range of field strengths where ionization is most probable and constrained to the neighborhood of directions perpendicular to the molecular axis and within the polarization plane. This is not what we observe.

Figure 11 shows the momentum distribution of the electrons in the molecular frame (i.e., with respect to the molecular axis which is set along the x' axis) and projected onto the x' - y'

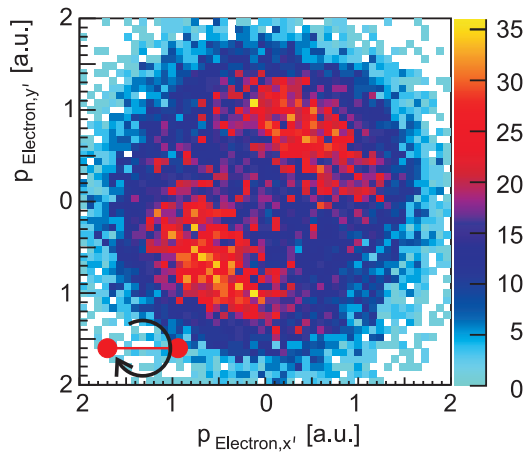


FIG. 11. (Color online) Electron momentum distribution in the molecular frame projected onto the polarization plane for 40-fs, $6 \times 10^{14} \text{ W cm}^{-2}$ circularly polarized laser pulses. The sense of rotation is clockwise, as indicated in the bottom left-hand corner. The molecular axis is orientated along the x' axis (from [18]).

polarization plane. Measurements were performed with 40-fs, $I = 6 \times 10^{14} \text{ W cm}^{-2}$ laser pulses, leading to an expected maximum momentum of 1.6 a.u. The laser helicity was clockwise. All references to angles made in this section refer to this sense of rotation and are measured with respect to the expected emission direction perpendicular to the molecular axis. In contrast to expectations based upon the free-electron model, the distribution is tilted by an angle of about 40° from the y' axis and exhibits a broad range of absolute values for electron momenta, tending to much smaller values than anticipated.

An alternative rendering of our data is shown in Fig. 12, where the ionization rate is shown as a function of the magnitude of the electron momenta components within the polarization plane p_{\parallel} ($p_{\parallel} = \sqrt{p_x'^2 + p_y'^2}$) and perpendicular to the polarization plane p_{\perp} ($=p_z$) for the case where the molecular axis is confined to the polarization plane. A much larger range of values is observed for the momentum component within the plane relative to those for the component perpendicular to the plane. A nonzero range of values for p_{\perp} is observed, which is not anticipated in the free-electron model.

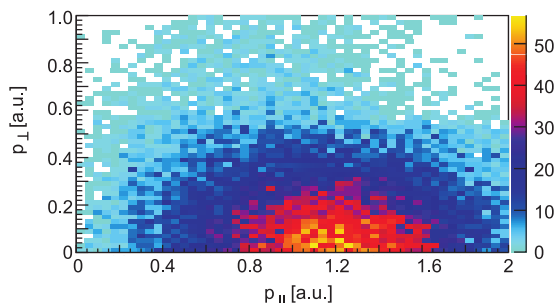


FIG. 12. (Color online) Electron momentum distribution showing the dependence of electron counts on the magnitude of the components of electron momenta within (p_{\parallel}) and perpendicular to (p_{\perp}) the polarization plane.

In the quasistatic description of strong-field ionization the ionization rate depends on only the intensity, the wavelength, and the angle of the electric field with the molecular axis at the instant of ionization. A maximum ionization rate is expected when the barriers of the combined nuclei become thinnest or lowest, which coincides with maximum field projections along the internuclear axis. Excluding the postemission interaction of the electron with the nuclei and assuming zero momentum of the emitted electron at the tunnel exit, the quasistatic description predicts that the action of the laser would lead to a symmetric distribution about the y' axis. Since the measured distribution in Fig. 11 does not show such a symmetry, this suggests that aspects of the dynamical nature of the process beyond those treated in the quasistatic approaches need to be considered. Furthermore, the finite width of the distribution of the momentum component out of the polarization plane evident in Fig. 12 suggests that an initial momentum distribution with nonzero width exists at the tunnel exit, which cannot be neglected. These conclusions are supported by recent quantum simulations [18,21,22] which describe the evolution of the electron wave function in the nuclear and laser fields. They show that ionization is a dynamical process which does not happen instantaneously but is extended over a finite time. In these calculations the electron, driven by the laser field, leaves the molecule with a finite value of momentum before the Coulomb explosion occurs, with a value dependent on the phase of the laser field within the molecular frame at the time of release. When the electron has finally reached a sufficient distance from the nuclei to neglect their mutual Coulombic attraction, the electric field has rotated farther on, further modifying the asymptotic electron-emission direction. Moreover, the calculations show the existence of transient laser-driven intramolecular electron transfer between the uphill and downhill sites, which occurs on the sub-laser-cycle time scale and leads to multiple bursts of ionization with a laser cycle. A further strong effect leading to the observed rotation is the interaction of the escaping electron with the ion field [52,53]. These effects combined are largely able to account for the angular structure and the breaking of reflection symmetry observed in Fig. 11 [18]. Moreover, as the instantaneous phase of the laser field (modulo 2π) is encoded in the emission direction of the electron within the molecular frame (the field rotates with approximately $138^\circ/\text{fs}$), the angular distribution of Fig. 11 provides a powerful window to quantify and calibrate subcycle emission processes on an attosecond time scale.

An experimental measure of the momentum distribution at the tunnel exit is provided by Fig. 13, which shows the distribution of values for p_{\perp} , the component of momentum measured along the axis perpendicular to the polarization plane. As stated in Sec. I, rescattering of the tunnel electron from the nuclei cannot occur for circular polarization but may occur under certain circumstances for linear polarization. Comparing Fig. 8(b), the distribution for the linearly polarized momentum component perpendicular to the polarization axis, to Fig. 13, one observes that while small differences in the wings of the two peaks are apparent, the half widths of both are essentially the same. The similarity between the two distributions suggests that for both cases the distributions accurately reflect the electron momentum components at

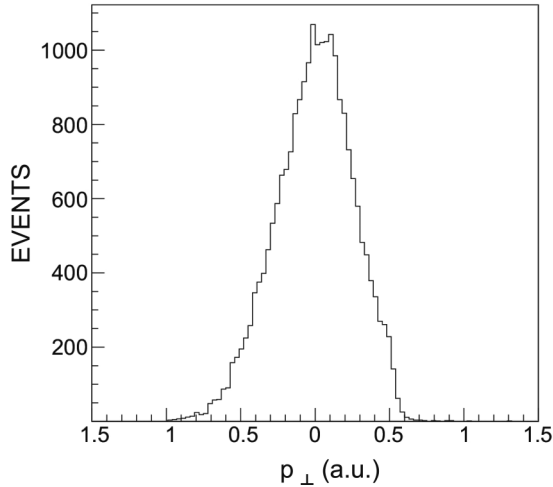


FIG. 13. Distribution of the momentum component of the emitted tunnel electron along an axis perpendicular to the polarization plane.

the tunnel exit and that, for linear polarization, rescattering from the nuclei does not lead to significant modifications to the momentum distribution under the adopted experimental conditions.

In Fig. 14 the dependency of the absolute value of the electron momenta on the KER and on the ascribed internuclear separation is presented. KER values below 2 eV (large internuclear separations) are not shown because of the high levels of proton background in this kinematic region resulting from dissociation. An upward tilt of the momentum distribution from left to right is apparent, with the trend for higher values of electron momentum to be associated with decreasing internuclear distance. Given that the electron energy (momentum) value is related to the laser intensity at the time of ionization, this trend suggests that ionization at small internuclear distances occurs at locations of higher instantaneous laser intensity within the pulse envelope. This behavior is opposite to the behavior which is observed for single photoionization in the limit of a weak laser field and that for multiphoton ionization and dissociation at 400 nm [54]: in

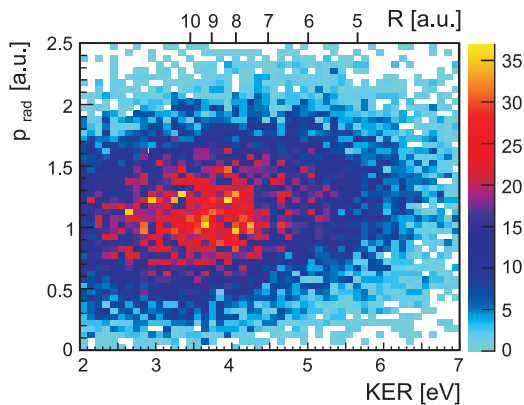


FIG. 14. (Color online) Dependence of the electron momentum component in the plane of polarization on the KER of the proton fragments. Internuclear separation values, ascribed according to the solid curve of Fig. 2, are shown on the top axis.

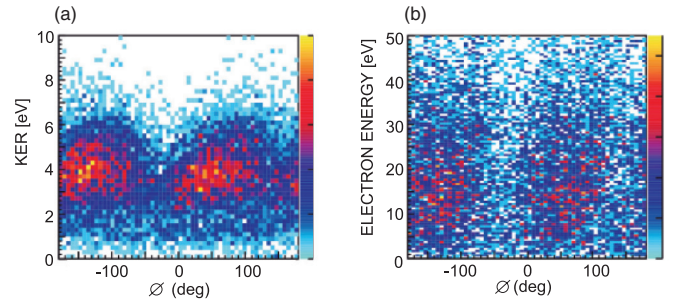


FIG. 15. (Color online) Dependence of the dissociative ionization rate on the angle between the electron momentum vector and the internuclear axis in the polarization plane and on (a) the KER and (b) the energy of the tunnel electron. Laser intensity $I \approx 6 \times 10^{14}$ W/cm².

that case, consistent with energy conservation, higher proton energies resulting from ionization at smaller internuclear distances are associated with *lower* electron energies.

In Fig. 11 we showed in momentum space that the angular distribution of the emitted tunnel electron was rotated in the polarization plane away from the molecular axis. An analogous breaking of symmetry in energy space is also observed within the polarization plane, as shown in Fig. 15, which depicts the dependencies of the KER of the proton fragments [Fig. 15(a)] and the energy of the tunnel electron [Fig. 15(b)] on the angle between the tunnel-electron momentum vector and the internuclear axis. In both plots a double-lobe structure is evident. The angular position of the lobes is seen to change with the KER of the proton fragments [Fig. 15(a)] and the energy of the tunnel electron [Fig. 15(b)]. Again, the distributions are not symmetric about the electron emission angle $\phi = 0^\circ$ and do not peak at $\phi = \pm 90^\circ$, as predicted by the free-electron model, but are rotated in emission angle. We note that for the symmetric fragmentation considered here all physical properties $f(\phi)$ must exhibit at inversion symmetry $f(\phi) = f(\phi + 180^\circ)$ within the polarization plane; reflection symmetry $f(\phi) = f(-\phi)$ would only be achieved if the property considered were not affected by the sense of angular momentum transfer to the system, which is not the case for all the results shown here.

IV. CONCLUSION

An H_2^+ ion in the presence of a laser field represents the simplest system in which to investigate fundamental properties of laser-molecule interactions. Here we present results from the world's first experiment analyzing the interaction of femtosecond laser pulses with hydrogen molecular ions by measuring the fragments (two protons and one electron) in a kinematically complete coincidence experiment. The full kinematic range of the process was explored by measuring protons and electrons over a full 4π acceptance solid angle. The study was rendered feasible by spatially separating electrons derived from H_2^+ ionization from those resulting from background-gas ionization, leading to an improvement of over two orders of magnitude in the ratio of signal to background events. The challenging requirement to accurately align an extremely diffuse target beam with the laser focus was overcome through

the development of a beam-monitoring system which can additionally evaluate the intensity of a laser pulse.

Due to a precursor dissociation process occurring at low laser intensities and on the rising edge of the laser pulse, we found that H_2^+ ions laser ionize at large internuclear separations corresponding to critical distances expected for the ionization-enhancing CREI process. For linearly polarized laser light the measured KER distribution shows an increased ionization rate above 5 a.u. that reaches its maximum at 10 a.u., consistent with the interpretation that CREI is the dominant process driving ionization. The angular distribution for proton emission is found to be confined to a small angular region around the polarization axis, and electron momenta show almost no dependency on the ascribed internuclear separation at the instant of ionization. For a circularly polarized laser field we extracted electron angular distributions within the polarization plane, referenced to the molecular axis, for different values of KER (corresponding to different internuclear separations at the tunnel exit) and for different values of electron momenta. In

contrast to expectations based upon the free-electron model, an unexpected rotation of the electron distributions away from the molecular axis was observed, accompanied by a broad range of absolute values for electron momenta, tending to much smaller values than anticipated. A previous comparison [18] of some of these results with calculations based on a solution of the time-dependent Schrödinger equation suggests a dynamic interplay between the rotating laser field, the Coulombic force of the nuclei, and the orbital structure of the electrons is at play, involving delayed ionization processes and a complex time structure at the attosecond time scale.

ACKNOWLEDGMENTS

This project was supported by the Deutsche Forschungsgemeinschaft. We thank K. Stiebing, P. Ziel, M. Dworak, and W. Dilfer for providing a high-quality ion beam.

-
- [1] H. Akagi, T. Otobe, A. Staudte, A. Shiner, F. Turner, R. Dörner, D. M. Villeneuve, and P. B. Corkum, *Science* **325**, 1364 (2009).
- [2] M. Meckel, D. Comtois, D. Zeidler, A. Staudte, D. Pavičić, H. C. Bandulet, H. Pépin, J. C. Kieffer, R. Dörner, D. M. Villeneuve, and P. B. Corkum, *Science* **320**, 1478 (2008).
- [3] Shih-I. Chu and J. Cooper, *Phys. Rev. A* **32**, 2769 (1985).
- [4] S. Chelkowski, A. Conjusteau, T. Zuo, and A. D. Bandrauk, *Phys. Rev. A* **54**, 3235 (1996).
- [5] M. Plummer and J. F. McCann, *J. Phys. B* **29**, 4625 (1996).
- [6] M. Plummer and J. F. McCann, *J. Phys. B* **30**, L401 (1997).
- [7] A. D. Bandrauk and H. Z. Lu, *Phys. Rev. A* **62**, 053406 (2000).
- [8] S. Chelkowski, C. Foisy, and A. D. Bandrauk, *Phys. Rev. A* **57**, 1176 (1998).
- [9] B. Feuerstein and U. Thumm, *Phys. Rev. A* **67**, 043405 (2003).
- [10] T. K. Kjeldsen, L. B. Madsen, and J. P. Hansen, *Phys. Rev. A* **74**, 035402 (2006).
- [11] F. Li, T. Wang, G. Zhang, W. Xiang, and W. T. Hill, *Chin. Phys. Lett.* **25**, 465 (2008).
- [12] N. P. F. B. van Asselt, J. G. Maas, and J. Los, *Chem. Phys.* **5**, 429 (1974).
- [13] G. N. Gibson, M. Li, C. Guo, and J. Neira, *Phys. Rev. Lett.* **79**, 2022 (1997).
- [14] Th. Ergler, A. Rudenko, B. Feuerstein, K. Zrost, C. D. Schröter, R. Moshhammer, and J. Ullrich, *Phys. Rev. Lett.* **95**, 093001 (2005).
- [15] D. Pavičić, A. Kiess, T. W. Hänsch, and H. Figger, *Phys. Rev. Lett.* **94**, 163002 (2005).
- [16] P. Q. Wang, A. M. Sayler, K. D. Carnes, J. F. Xia, M. A. Smith, B. D. Esry, and I. Ben-Itzhak, *Phys. Rev. A* **74**, 043411 (2006).
- [17] I. Ben-Itzhak, P. Q. Wang, A. M. Sayler, K. D. Carnes, M. Leonard, B. D. Esry, A. S. Alnaser, B. Ulrich, X. M. Tong, I. V. Litvinyuk, C. M. Maharjan, P. Ranitovic, T. Osipov, S. Ghimire, Z. Chang, and C. L. Cocke, *Phys. Rev. A* **78**, 063419 (2008).
- [18] M. Odenweller, N. Takemoto, A. Vredenburg, K. Cole, K. Pahl, J. Titze, L. Ph. H. Schmidt, T. Jahnke, R. Dörner, and A. Becker, *Phys. Rev. Lett.* **107**, 143004 (2011).
- [19] T. Zuo and A. D. Bandrauk, *Phys. Rev. A* **52**, R2511 (1995).
- [20] J. Wu, M. Meckel, L. Ph. H. Schmidt, M. Kunitski, S. Voss, H. Sann, H. Kim, T. Jahnke, A. Czasch, and R. Dörner, *Nat. Commun.* **3**, 1113 (2012).
- [21] N. Takemoto and A. Becker, *Phys. Rev. Lett.* **105**, 203004 (2010).
- [22] N. Takemoto and A. Becker, *Phys. Rev. A* **84**, 023401 (2011).
- [23] P. B. Corkum, *Phys. Rev. Lett.* **71**, 1994 (1993).
- [24] P. B. Corkum, N. H. Burnett, and F. Brunel, *Phys. Rev. Lett.* **62**, 1259 (1989).
- [25] See H. B. van Linden van den Heuvell and Muller, in *Multiphoton Processes*, edited by S. J. Smith and P. L. Knight (Cambridge University Press, Cambridge 1988), where they give the name “Simpleman” theory to a classical description of electron motion resulting solely through the action of the laser field. Such a theory is one in a class of theories of electrons in plane-wave radiation fields. For a review, see J. H. Eberly, *Prog. Opt.* **7**, 359 (1969). Results generated from the solution of time-dependent Newton equations extending beyond the free-electron approach have recently been presented by Xu Wang and J. H. Eberly, *Phys. Rev. A* **86**, 013421 (2012).
- [26] P. Eckle, A. N. Pfeiffer, C. Cirelli, A. Staudte, R. Dörner, H. G. Muller, M. Büttiker, and U. Keller, *Science* **322**, 1525 (2008).
- [27] A. Staudte, S. Patchkovskii, D. Pavičić, H. Akagi, O. Smirnova, D. Zeidler, M. Meckel, D. M. Villeneuve, R. Dörner, M. Yu. Ivanov, and P. B. Corkum, *Phys. Rev. Lett.* **102**, 109901(E) (2009).
- [28] J. Wu, M. Magrakvelidze, L. P. H. Schmidt, M. Kunitski, T. Pfeifer, M. Schöffler, M. Pitzer, M. Richter, S. Voss, H. Sann, H. Kim, J. Lower, T. Jahnke, A. Czasch, U. Thumm, and R. Dörner, *Nat. Commun.* **4**, 2177 (2013).
- [29] A. Giusti-Suzor, X. He, O. Atabek, and F. H. Mies, *Phys. Rev. Lett.* **64**, 515 (1990).
- [30] P. H. Bucksbaum, A. Zavriyev, H. G. Muller, and D. W. Schumacher, *Phys. Rev. Lett.* **64**, 1883 (1990).
- [31] A. Giusti-Suzor and F. H. Mies, *Phys. Rev. Lett.* **68**, 3869 (1992).
- [32] G. Jolicard and O. Atabek, *Phys. Rev. A* **46**, 5845 (1992).

- [33] K. C. Kulander, F. H. Mies, and K. J. Schafer, *Phys. Rev. A* **53**, 2562 (1996).
- [34] J. Ludwig, H. Rottke, and W. Sandner, *Phys. Rev. A* **56**, 2168 (1997).
- [35] A. Datta, S. Saha, and S. S. Bhattacharyya, *J. Phys. B* **30**, 5737 (1997).
- [36] L. J. Frasinski, J. H. Posthumus, J. Plumridge, K. Codling, P. F. Taday, and A. J. Langley, *Phys. Rev. Lett.* **83**, 3625 (1999).
- [37] K. Sändig, H. Figger, and T. W. Hänsch, *Phys. Rev. Lett.* **85**, 4876 (2000).
- [38] L. J. Frasinski, J. Plumridge, J. H. Posthumus, K. Codling, P. F. Taday, E. J. Divall, and A. J. Langley, *Phys. Rev. Lett.* **86**, 2541 (2001).
- [39] L.-Y. Peng, I. D. Williams, and J. F. McCann, *J. Phys. B* **38**, 1727 (2005).
- [40] J. J. Hua and B. D. Esry, *Phys. Rev. A* **78**, 055403 (2008).
- [41] J. McKenna, A. M. Sayler, F. Anis, B. Gaire, N. G. Johnson, E. Parke, J. J. Hua, H. Mashiko, C. M. Nakamura, E. Moon, Z. Chang, K. D. Carnes, B. D. Esry, and I. Ben-Itzhak, *Phys. Rev. Lett.* **100**, 133001 (2008).
- [42] L. Ph. H. Schmidt, T. Jahnke, A. Czasch, M. Schöffler, H. Schmidt-Böcking, and R. Dörner, *Phys. Rev. Lett.* **108**, 073202 (2012).
- [43] J. R. Pierce, *Theory and Design of Electron Beams*, 2nd ed. (Van Nostrum, New York, 1954).
- [44] D. M. Villeneuve, I. Fischer, A. Zavriyev, and A. Stolow, *J. Chem. Phys.* **107**, 5310 (1997).
- [45] G. H. Dunn, *J. Chem. Phys.* **44**, 2592 (1966).
- [46] R. Dörner, V. Mergel, O. Jagutzki, L. Spielberger, J. Ullrich, R. Moshammer, and H. Schmidt-Böcking, *Phys. Rep.* **330**, 95 (2000).
- [47] O. Jagutzki, A. Cerezo, A. Czasch, R. Dörner, M. Hattas, M. Min Huang, V. Mergel, U. Spillmann, K. Ullmann-Pfeger, T. Weber, H. Schmidt-Böcking, and G. D. W. Smith, *IEEE Trans. Nucl. Sci.* **49**, 2477 (2002).
- [48] O. Jagutzki, V. Mergel, K. Ullmann-Pfeger, L. Spielberger, U. Spillmann, R. Dörner, and H. Schmidt-Böcking, *Nucl. Instrum. Methods Phys. Res., Sect. A* **477**, 244 (2002).
- [49] I. Ben-Itzhak, in *Fragmentation Processes*, edited by Colm T. Whelan (Cambridge University Press, Cambridge, 2013), p. 72.
- [50] N. B. Delone and V. P. Krainov, *J. Opt. Soc. Am. B* **8**, 1207 (1991).
- [51] L. Arissian, C. Smeenk, F. Turner, C. Trallero, A. V. Sokolov, D. M. Villeneuve, A. Staudte, and P. B. Corkum, *Phys. Rev. Lett.* **105**, 133002 (2010).
- [52] M. Spanner, S. Gräfe, S. Chelkowski, D. Pavičić, M. Meckel, D. Zeidler, A. B. Bardon, B. Ulrich, A. D. Bandrauk, D. M. Villeneuve, R. Dörner, P. B. Corkum, and A. Staudte, *J. Phys. B* **45**, 194011 (2012).
- [53] J. Wu, M. Meckel, S. Voss, H. Sann, M. Kunitski, L. Ph. H. Schmidt, A. Czasch, H. Kim, T. Jahnke, and R. Dörner, *Phys. Rev. Lett.* **108**, 043002 (2012).
- [54] J. Wu, M. Kunitski, M. Pitzer, F. Trinter, L. Ph. H. Schmidt, T. Jahnke, M. Magrakvelidze, C. B. Madsen, L. B. Madsen, U. Thumm, and R. Dörner, *Phys. Rev. Lett.* **111**, 023002 (2013).